fluids

MDPI

Article

Near Real-Time Estimation of Blood Loss and Flow–Pressure Redistribution during Unilateral Nephrectomy

James Cowley [1,*], Justicia Kyeremeh [2], Grant D. Stewart [2], Xichun Luo [3], Wenmiao Shu [1] and Asimina Kazakidi [1,*]

[1] Department of Biomedical Engineering, University of Strathclyde, Glasgow G4 0NW, UK
[2] Department of Surgery, University of Cambridge, Cambridge CB2 0QQ, UK
[3] Centre for Precision Manufacturing, Department of Design Manufacturing & Engineering Management, University of Strathclyde, Glasgow G1 1XJ, UK
* Correspondence: james.cowley.100@strath.ac.uk (J.C.); asimina.kazakidi@strath.ac.uk (A.K.)

Abstract: Radical or partial nephrectomy, commonly used for the treatment of kidney tumors, is a surgical procedure with a risk of high blood loss. The primary aim of this study is to quantify blood loss and elucidate the redistribution of blood flux and pressure between the two kidneys and the abdominal aorta during renal resection. We have developed a robust research methodology that introduces a new lumped-parameter mathematical model, specifically focusing on the vasculature of both kidneys using a non-Newtonian Carreau fluid. This model, a first-order approximation, accounts for the variation in the total impedance of the vasculature when various vessels are severed in the diseased kidney (assumed to be the left in this work). The model offers near real-time estimations of the flow–pressure redistribution within the vascular network of the two kidneys and the downstream aorta for several radical or partial nephrectomy scenarios. Notably, our findings indicate that the downstream aorta receives an approximately 1.27 times higher percentage of the redistributed flow from the diseased kidney compared to that received by the healthy kidney, in nearly all examined cases. The implications of this study are significant, as they can inform the development of surgical protocols to minimize blood loss and can assist surgeons in evaluating the adequacy of the remaining kidney vasculature.

Keywords: blood loss; kidney tumor; renal arteries; vessel cutting; surgery; resection; two-kidney vasculature; simulation; mathematical modelling; lumped-parameter model; blood flux; pressure

check for updates

Citation: Cowley, J.; Kyeremeh, J.; Stewart, G.D.; Luo, X.; Shu, W.; Kazakidi, A. Near Real-Time Estimation of Blood Loss and Flow–Pressure Redistribution during Unilateral Nephrectomy. *Fluids* **2024**, *9*, 214. https://doi.org/10.3390/fluids9090214

Academic Editor: D. Andrew S. Rees

Received: 24 July 2024
Revised: 6 September 2024
Accepted: 10 September 2024
Published: 13 September 2024

Copyright: © 2024 by the authors. Licensee MDPI, Basel, Switzerland. This article is an open access article distributed under the terms and conditions of the Creative Commons Attribution (CC BY) license (https://creativecommons.org/licenses/by/4.0/).

1. Introduction

Renal cancer is responsible for more than 2% of new cancer cases worldwide, affecting over 330,000 individuals annually. Primary surgical interventions for this form of cancer include radical nephrectomy and partial nephrectomy, which can be performed laparoscopically or through open surgery. Recently, robotic-assisted partial nephrectomy has gained considerable prominence and is regarded as a gold standard in the field.

Radical or partial nephrectomy for the treatment of kidney tumors is a surgical procedure with a substantial risk of bleeding due to cutting of various blood vessels in complex renal vascular networks. Effective management of blood loss during renal surgery is crucial for minimizing surgical trauma. A clinical study by Rosiello et al. [1] identified a link between blood losses larger than 500 mL and the risk of chronic kidney disease. Other studies highlighted the association between general surgery and chronic kidney disease [2–5]. Jaramillo et al. [6] emphasized the necessity of more precise techniques to accurately measure blood loss and stressed the limits and inaccuracies of in vivo measurements alongside the use of empirical algorithms. A comprehensive understanding of kidney vascular perfusion and blood loss during renal surgery may help surgeons improve the recovery times of patients by reducing the risk of bleeding and potential trauma. However, the scale and

complexity of the vascular networks within each of the kidneys make this task particularly challenging.

The kidneys' vascular networks have complex structure with multiple interconnected blood vessels and branching points, commonly dividing into two, three, four, or five branches. Central to the understanding of the anatomy of renal vasculature is rigorous clinical data obtained using various medical imaging techniques, such as optical projection tomography (OPT) as discussed by Puelles et al. [7] and magnetic resonance imaging, MRI (e.g., as presented by Schutter et al. [8]). Nordsletten et al. [9] developed an automated segmentation technique to construct rat kidney vessel morphology from micro-computed tomography (μCT) images, while Kalantarinia et al. [10] imaged the kidney vascular structure via high-frequency ultrasound in conjunction with ultrasound contrast agents, UCAs [11,12].

According to Lok et al. [13], a typical healthy human kidney exhibits a blood flow rate of 600 mL/min, with both kidneys, combined, requiring approximately 25% of the cardiac output (CO) which amounts to about 5000 mL/min. Various studies have considered renal hemodynamics and autoregulation of blood flow in human and animal models [14–31]. Furthermore, key insights concerning physiological blood flow in the renal arteries have been provided by several numerical simulations [32–36]. For example, Cury et al. [32] considered a numerical simulation of a single human kidney's vasculature, whereas Postnov et al. [37] developed a mathematical model of a single renal vascular network using a probability-based topological method. Additionally, Hao et al. [38] derived a mathematical model for renal fibrosis, while Basri et al. [39] designed a computational fluid dynamic simulation of stenotic renal arteries. There are a plethora of other studies on computational and mathematical modelling of various vascular networks [40–43], as well as several numerical approaches that study diverse vascular geometries [44–52]. However, as far as the authors are aware, there appears to be no other existing mathematical model or simulation from any research groups that can both estimate the perfusion in the vasculature of the two kidneys and simultaneously quantify the blood loss due to the severing of blood vessels during surgery, within a short timeframe.

The primary objective of the present study is to extend and expand the work of Cowley et al. [53], who derived a lumped-parameter first-approximation model of a single kidney vascular network to calculate the blood loss resulting from the cutting of several blood vessels. The novelty of this new article lies in the incorporation of both kidneys and the downstream abdominal aorta into the model, as well as the near real-time estimation of blood loss during partial and radical nephrectomy of one of the kidneys, before autoregulation and coagulation become relevant. This lumped-parameter, first-approximation mathematical model accounts for the variation in the total impedance of the two-kidney system and efficiently estimates the blood flow redistribution following a range of vessel cuts due to surgery. The developed algorithms can be translated into a clinical environment and can be adapted to a specific case of an individual patient. Consequently, this study provides a modelling framework for pre-operative planning of various surgical nephrectomy scenarios.

The remainder of this article consists of, first, a Methods section (Section 2) where model assumptions and methodology are described. This is followed by a Results section (Section 3), where findings are presented diagrammatically. The Discussion section (Section 4) discusses the modelling results and their implications on renal surgery. The limitations of the model are highlighted, and a future research vision is also discussed.

2. Methods

2.1. The Renal Vasculature

A complex vascular network of the two kidneys and abdominal aorta (Figure 1) was created for this study, based on the optical projection tomography image of a single kidney by Puelles et al. [7] and by extending our previous single-kidney vasculature (Figure 2) [53]. The authors assumed that both the left and right kidney have identical geometrical structure

as well as physical parameters and are connected to the aorta via a trifurcation node (Figure 1). For simplicity, the superior mesenteric artery was ignored. Individually, the left and right kidney were each considered an asymmetric vascular network composed of 25 vascular branching nodes (represented as black circles in Figure 1) and 61 blood vessels (illustrated by line segments) and organized into left ("L") and right ("R") branches relative to the first bifurcation node of each of the main (left or right) renal arteries and the two primary daughter vessels of each kidney; thus labelled as LL1 (to indicate the first left branch of the left renal artery) and LR1 (the first right branch of the left renal artery) for the left kidney and RL1 (the first left branch of the right renal artery) and RR1 (the first right branch of the right renal artery) for the right kidney (Figure 1).

The radii for the main left and right arterial branches (LL1–LR1, RL1–RR1) were determined following Murray's law [54], while the radii for the remaining vessels (LL2–LL23 and LR2–LR38, RL2–RL23 and RR2–RR38) were variable based on measurements by [32]. Cury et al. [32] showed that the arteries of the kidney are of a similar order of magnitude in length, so for simplicity, we considered all the blood vessels in our vascular network to be of equal length. We further assumed cylindrical vessel segments with uniform cross-sections and that the branching angles at each node were negligible, based on a previous study by Yang et al. [55].

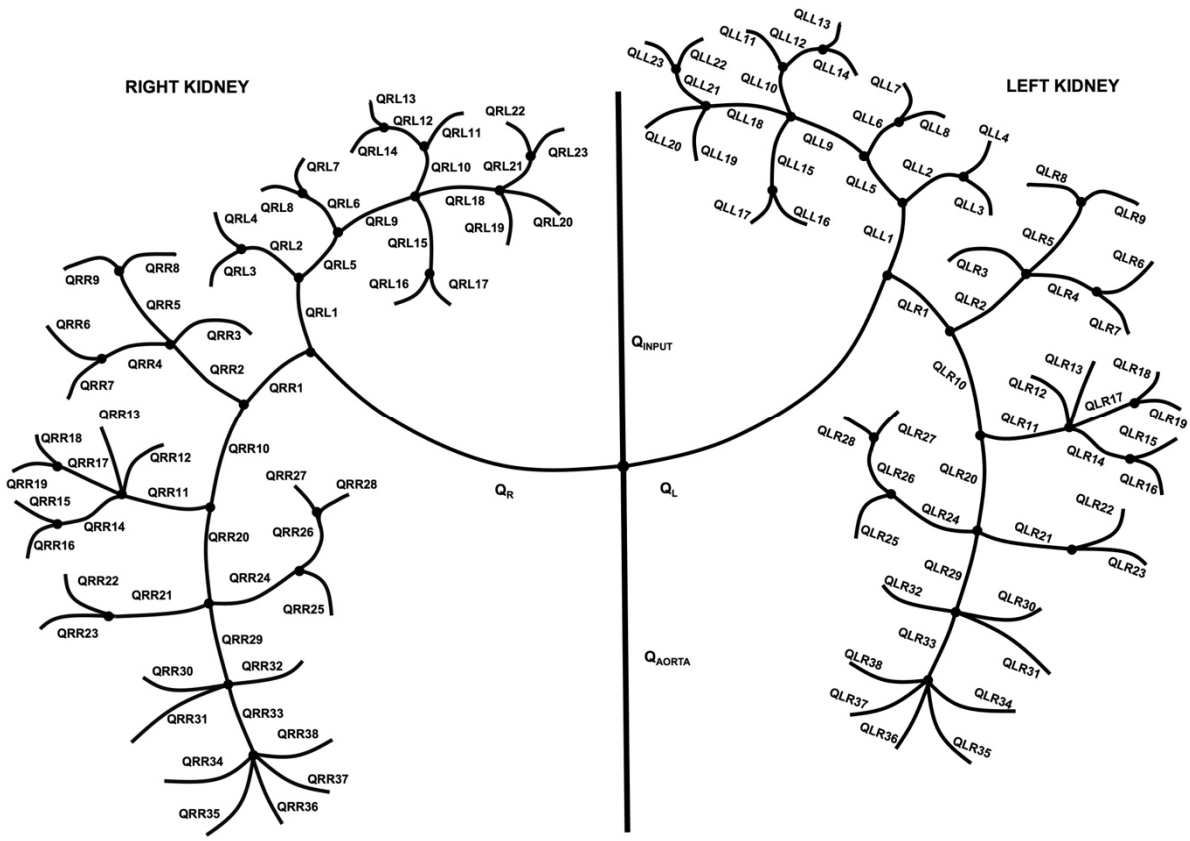

Figure 1. Schematic of the vascular network model assumed for the two kidneys and abdominal aorta. The left and right kidney were considered identical in structure and their major renal arteries Q_R and Q_L joined the aorta at a single location. For simplicity, the superior mesenteric artery was ignored. Each kidney was represented by an asymmetric vascular network composed of 25 vascular branching nodes (black circles) and 61 blood vessels (line segments) and organized into left ("L") and right ("R") branches relative to the first bifurcation node of each of the main renal arteries. The blood vessels of the left kidney were labelled as (LL1–LL23 and LR1–LR38), while those of the right kidney were labelled as (RL1–RL23 and RR1–RR38). See text for further details.

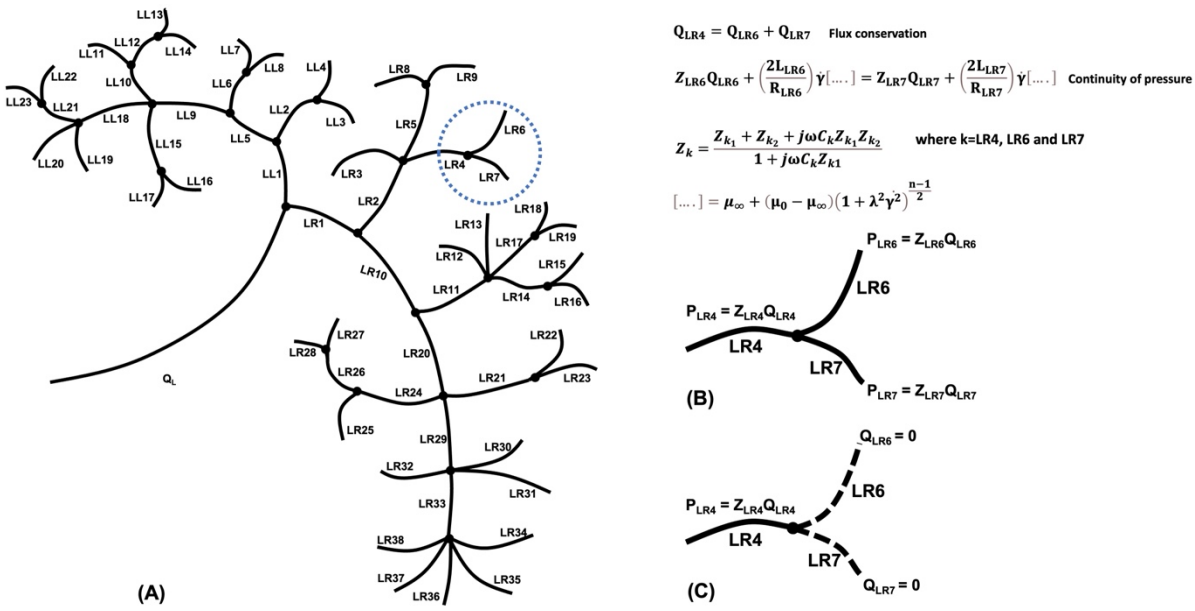

Figure 2. (**A**) The vascular network for the human left kidney. The blue circle indicates an example of a bifurcation, where the blood vessel LR4 divides into the vessels LR6 and LR7, shown in more detail in (**B**) the healthy case and (**C**) a partial nephrectomy scenario where the branches LR6 and LR7 are cut. The presented first-approximation lumped-parameters model assumes that each vessel has an impedance described by (**B**) the three-element Windkessel model, with two resistors Z_{k1} and Z_{k2} and a compliance C_k of the blood vessel. (**C**) The model also considers that each cut (severed) blood vessel has a zero output flux (modified from [53]).

2.2. Mathematical Approximations

The new two-kidney lumped-parameter mathematical model is an extension of the model presented in [53], using similar numerical assumptions. In brief: (a) The blood was modelled as an incompressible fluid using the Carreau non-Newtonian model [56] since it accounts for the shear-thinning behavior of blood, giving control over different shear rates. (b) The flow was considered laminar and quasi-steady [57], with the pulsations of blood flow being neglected. (c) The influence of backflow, associated with reflected waves due to the propagation of the arterial pulse wave through the vessels, was considered negligible, as demonstrated in the sensitivity analysis conducted in [53] for a single kidney, and was, therefore, neglected. (d) The inlet flow rate in the abdominal aorta, Q_{aorta}, was assumed 2400 mL/min [13,58]. (e) The hematocrit, φ, was taken equal to the physiological value of 0.4 [59]. (f) The blood vessels were assumed to be rigid, and any viscoelastic physical characteristics were neglected. (g) The blood vessels that were severed had zero blood flow and pressure, and any remaining uncut output blood vessels possessed a constant pressure described by Ohm's Law (see Figure 2C). (h) Both kidneys were assumed to be physically identical and connected to the abdominal aorta via a common node (Figure 1).

Referring to Figure 2B as an example, where the vessel LR4 divides into the blood vessels LR6 and LR7 we apply the conservation of flux and the continuity of pressure at each branching node of the two-kidney model to systematically solve the equations:

$$Q_{LR4} = Q_{LR6} + Q_{LR7} \tag{1}$$

$$P_{LR6} + \Delta P_{LR6} = P_{LR7} + \Delta P_{LR7} \tag{2}$$

where Q_k is the flux (here k = LR4, LR6, LR7); ΔP_k is the pressure gradient; and P_k is the pressure, written as a time (t)- and angular frequency (ω)-dependent function $P_k = P_0 \exp(j\omega t)$ with P_0 representing the pressure amplitude and given by Ohm's Law $P_k = Z_k Q_k$, where Z_k is the impedance of the blood vessel.

The magnitude of the total impedance, Z_k, of each individual blood vessel of the network (where k = LL1, . . .LL23, LR1, . . .LR38) for the left and right kidneys of the two-kidney vasculature was calculated using the three-element Windkessel model [41] and circuit theory, as [53]:

$$Z_k = \frac{Z_{k_1} + Z_{k_2} + j\omega C_k Z_{k_1} Z_{k_2}}{1 + j\omega C_k Z_{k1}}. \quad (3)$$

where Z_{k1}, Z_{k2} are resistors, and $C_k = \Delta V_k / \Delta P_k$ is a capacitor representing the compliance of each blood vessel; ΔV_k is the change in vessel volume. The impedance of the compliance, denoted by Z_{Ck}, is $Z_{Ck} = 1/j\omega C_k$. The vessel flux, Q_k, can be expressed as $Q_k = C_k dP_k/dt = j\omega C_k P_k$.

The viscosity was modelled using a Carreau fluid model (Supplementary Materials, Equation (S1)) in conjunction with the physical parameters found in [56,60]. Using the flux conservation at the example bifurcation node splitting to LR6 and LR7 vessels (Figure 2B), the pressure in each daughter branch is equated to give:

$$P^\star = Z_{LR6}Q_{LR6} + \left(\frac{2L_{LR6}}{R_{LR6}}\right)\dot{\gamma}\left[\mu_\infty + (\mu_0 - \mu_\infty)\left(1 + \lambda^2\dot{\gamma}^2\right)^{\frac{n-1}{2}}\right] = Z_{LR7}Q_{LR7} + \left(\frac{2L_{LR7}}{R_{LR7}}\right)\dot{\gamma}\left[\mu_\infty + (\mu_0 - \mu_\infty)\left(1 + \lambda^2\dot{\gamma}^2\right)^{\frac{n-1}{2}}\right]. \quad (4)$$

Equation (5) can be rearranged to:

$$Z_{LR6}Q_{LR6} - Z_{LR7}(Q_{LR4} - Q_{LR6}) + 2\dot{\gamma}\left(\frac{L_{LR6}}{R_{LR6}} - \frac{L_{LR7}}{R_{LR7}}\right)\left[\mu_\infty + (\mu_0 - \mu_\infty)\left(1 + \lambda^2\dot{\gamma}^2\right)^{\frac{n-1}{2}}\right] = 0. \quad (5)$$

Equation (5) can be solved for Q_{LR6} since the total flux Q_{LR4} is known as well as the impedances (Z_{LR6} and Z_{LR7}), the lengths of the vessels (L_{LR6} and L_{LR7}), the radii (R_{LR6} and R_{LR7}), and the viscosity for a specified shear strain rate. Further details on the mathematical approximations and a sensitivity analysis can be found in the Supplementary Materials of [53].

2.3. Modelling Cuts to the Two-Kidney Vascular Network

Due to the complexity of the two-kidney vascular structure, numerous cuts result in a new vascular arrangement which is a subset of the original vascular network. Every blood vessel cut creates a new, unique set of equations describing the flux conservation and the pressure continuity and yielding simultaneous equations that can be solved numerically using the platform Mathematica [61]. These distinct sets of algorithms account for the change in the total impedance of the vascular network due to surgical cuts. We verified computationally that the blood flux at each node was always conserved. The rest of this article will focus on various cuts to key primary and secondary vessels within our vascular network.

2.4. Verification and Validation

We have implemented the same methodological approach and validation techniques as Cowley et al. [53]. We validated our model by comparing our computations with the experimental results of Zhao and Lieber [62] and Shroter and Sudlow [63] for a Y junction, where we found differences of 3.4% and 3.6%, respectively. We also conducted a validation of the entire left kidney network based on the study of Jaramillo et al. [6]. They found a 3.64% mean blood volume loss in urological surgery patients with the use of the López-Picado formula [64] which was in good agreement with direct blood loss measurements, while our blood volume loss estimation of severing the Q_{LR2} and Q_{LR10} vessels was 2.46%. Using the same physical dimensions and flow conditions and assumptions, we further validated our modelling methodology for Y and T junctions as described in [46] yielding 1.1% and 1.6% differences, respectively, in the flow rates and pressures. This validates that the influence of different branching angles and unsteady flow is minimal in the model.

3. Results

3.1. Blood Flow Rates in a Healthy Two-Kidney Model

Let us consider first the blood flow in the healthy vasculature of a pair of kidneys, before discussing blood loss rates due to surgery. We calculated the blood fluxes in the healthy network by applying the flux conservation and the pressure continuity at each node via a system of linear equations, such as Equations (1) and (5), alongside the data from Tables S1 and S2 of the Supplementary Materials. The physical parameters for the two-kidney vascular network were obtained from previous studies [32,58,65,66]. Figure 3 illustrates the resulting distribution of blood flux in the healthy case.

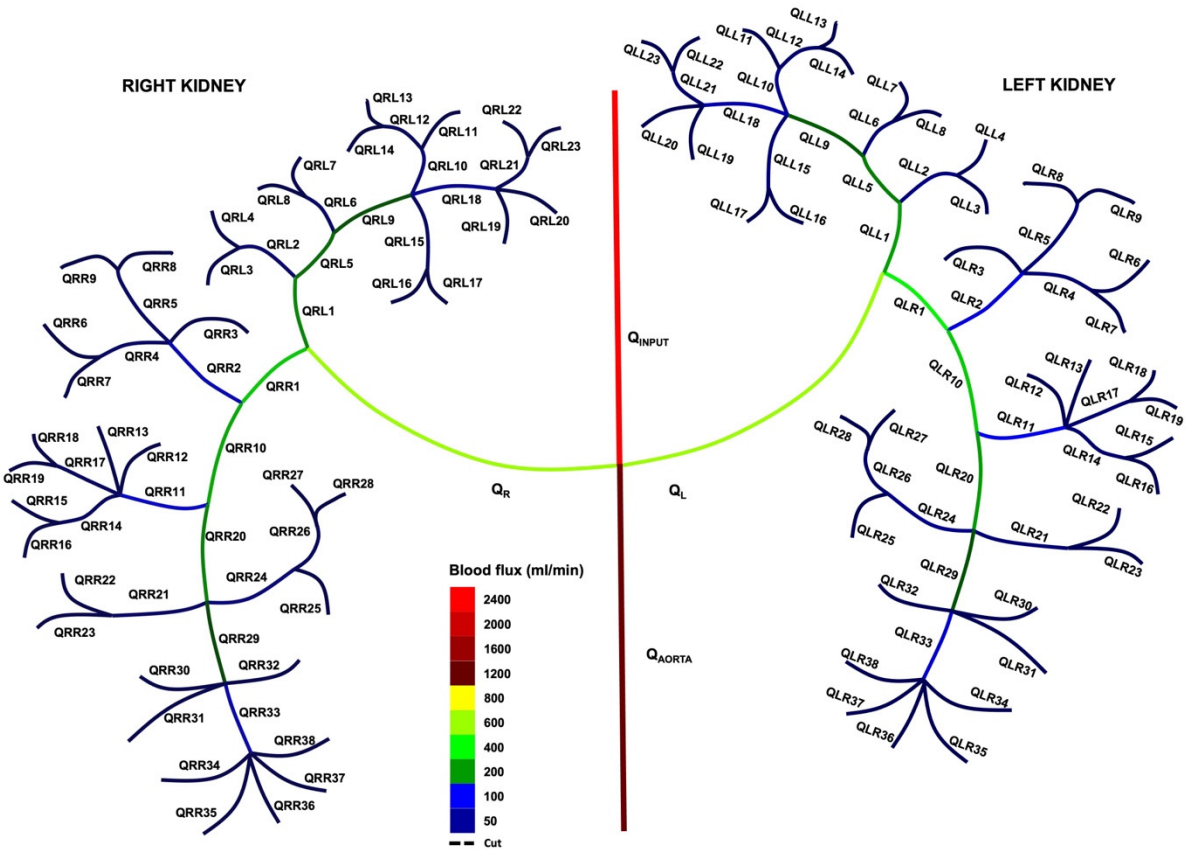

Figure 3. Schematic of the blood flux distribution for the healthy (uncut) two-kidney vascular network before any vessels in the left kidney are severed.

The blood fluxes to the healthy left and right renal arteries were $Q_L = Q_R = 599.6$ mL/min whereas the aorta arterial output had a blood flux of $Q_{aorta} = 1200.8$ mL/min. The downstream aorta had a greater blood flow rate since this is a large vessel with a wider radius delivering oxygen and nutrients to the periphery, and thus a lower impedance. The physiological blood fluxes in the left and right branches of the left kidney, Q_{LL1} and Q_{LR1}, were 212.5 mL/min and 387.1 mL/min, respectively, highlighting the asymmetry within each kidney and illustrating that the Q_{LL1} pathway had a larger impedance compared to the Q_{LR1} pathway.

3.2. Estimation of Blood Loss in Radical or Partial Unilateral Nephrectomy

We calculated the blood loss rates and blood fluxes for several different examples of single and double cuts to the blood vessels of a diseased kidney requiring radical or partial nephrectomy (here the left kidney was considered, but the results would be valid also for the right). We estimated the blood fluxes using the Carreau fluid model described by Equation (4), in conjunction with the flux conservation and the pressure continuity

(Equations (1) and (5)) and the physical data from Tables S1 and S2 (see Supplementary Materials). Each vessel's blood loss was recorded as a percentage of the total amount of blood (cardiac output, CO) in the typical 70 kg human body, considered as 5000 mL/min [13] (Table 1). It is worth noting that the % of blood loss in most partial nephrectomy scenarios with double or more cuts (representing a surgical resection of about half of the left kidney) was higher than that for a radical nephrectomy. The only case, from those shown in Table 1, where the % of blood loss was less was for a resection case with severed blood vessels at the bottom tip of the diseased (left) kidney (after vessel Q_{LR33}).

Table 1. Blood loss rates for various cuts to blood vessels for the Carreau fluid model.

Branch Cut(s)	Blood Loss from Individual Vessel (mL/min)	Total Blood Loss (mL/min)	% Blood Loss
Q_L (radical kidney nephrectomy)	59.9	59.9	1.20
Q_{LR33}	34.9	34.9	0.70
Q_{LR2} & Q_{LR10}	24.3 & 48.5	72.8	1.46
Q_{LR11} & Q_{LR20}	22.0 & 44.1	66.1	1.32
Q_{LL2} & Q_{LL5}	22.4 & 44.9	67.3	1.35
Q_{LL6} & Q_{LL9}	20.7 & 41.6	62.3	1.25
Q_{LL6} & Q_{LL9} & Q_{LR2} & Q_{LR10}	24.5 & 48.8 & 25.9 & 51.5	150.7	3.01

3.3. Redistribution of Blood Fluxes Due to Unilateral Kidney Nephrectomy

Table 2 illustrates the blood redistribution from the left kidney, undergoing radical or partial nephrectomy, to the right kidney and to the downstream abdominal aorta for various cuts to different blood vessels. The considered scenarios demonstrated that approximately 3–40% of Q_L was redistributed to the right kidney and 3–50% to the downstream abdominal aorta, with the downstream aorta receiving an approximately 1.27–1.28 times higher percentage of the redistributed flow than the right kidney in each case.

Table 2. Blood flux redistribution to the renal arteries and the downstream aorta for various cuts to different blood vessels.

Branch Cut(s)	Right Renal Artery Blood Flux, Q_R (mL/min)	% of Flow Redistributed from the Left Kidney to the Right	Left Renal Artery Blood Flux, Q_L (mL/min)	% of Flow Remaining at the Left Kidney	Downstream Aortic Blood Flux, Q_{aorta} (mL/min)	% of Flow Redistributed from the Left Kidney to Aorta	Ratio of Aortic to Right Kidney Redistribution
Healthy kidney (with no cuts)	599.6	-	599.6	-	1200.8	-	-
Q_L (radical left kidney nephrectomy)	837.7	39.71	59.9	9.99	1502.4	50.30	1.27
Q_{LR33} (partial left kidney nephrectomy)	613.2	2.27	568.6	94.83	1218.2	2.90	1.28
Q_{LR2} & Q_{LR10}	719.6	20.01	327.6	54.64	1352.8	25.35	1.27
Q_{LR11} & Q_{LR20}	685.0	14.24	406.0	67.71	1309	18.05	1.27
Q_{LL2} & Q_{LL5}	649.4	8.31	486.7	81.17	1263.9	10.52	1.27
Q_{LL6} & Q_{LL9}	637.4	6.30	513.8	85.69	1248.8	8.01	1.27
Q_{LL6} & Q_{LL9} & Q_{LR2} & Q_{LR10}	776.7	29.54	198.2	33.06	1425.1	37.41	1.27

Focusing on how surgery in a diseased kidney influences the blood flux rates to both the healthy kidney and the downstream aorta let us consider cuts after the nodes

Q_{LL6}, Q_{LL9}, Q_{LR2}, and Q_{LR10}, as represented by Figure 4. These cuts would result in the resection of a large portion of the outer regions of the left kidney (around the cortex and medulla), leaving intact the central region (the renal pelvis). The aorta's blood flux (Q_{aorta}) increased from 1200 mL/min to 1425.1 mL/min (18.68%), the healthy (right) kidney's Q_R increased from 599.6 mL/min to 776.7 mL/min (29.54%), while the left renal artery Q_L of the unhealthy kidney decreased substantially from 599.6 mL/min to 198.2 mL/min (by 66.94%). Therefore, it was found that 33.05% of the pre-surgical (healthy) left renal flow remained in the post-surgical resected kidney, while 37.41% of the pre-surgical flow was redirected to the downstream abdominal aorta and 29.54% to the right kidney (Table 2); that is, the aorta received 1.27 times more of the redistributed flow from the surgically-operated (left) kidney, which can be explained since the aorta has a larger radius and therefore a smaller impedance. The blood loss rates for each separate cut were Q_{LL6} = 24.5 mL/min, Q_{LL9} = 48.8 mL/min, Q_{LR2} = 25.9 mL/min, and Q_{LR10} = 51.5 mL/min, yielding a total blood loss rate of 150.7 mL/min, equivalent to 3% of the average human cardiac output.

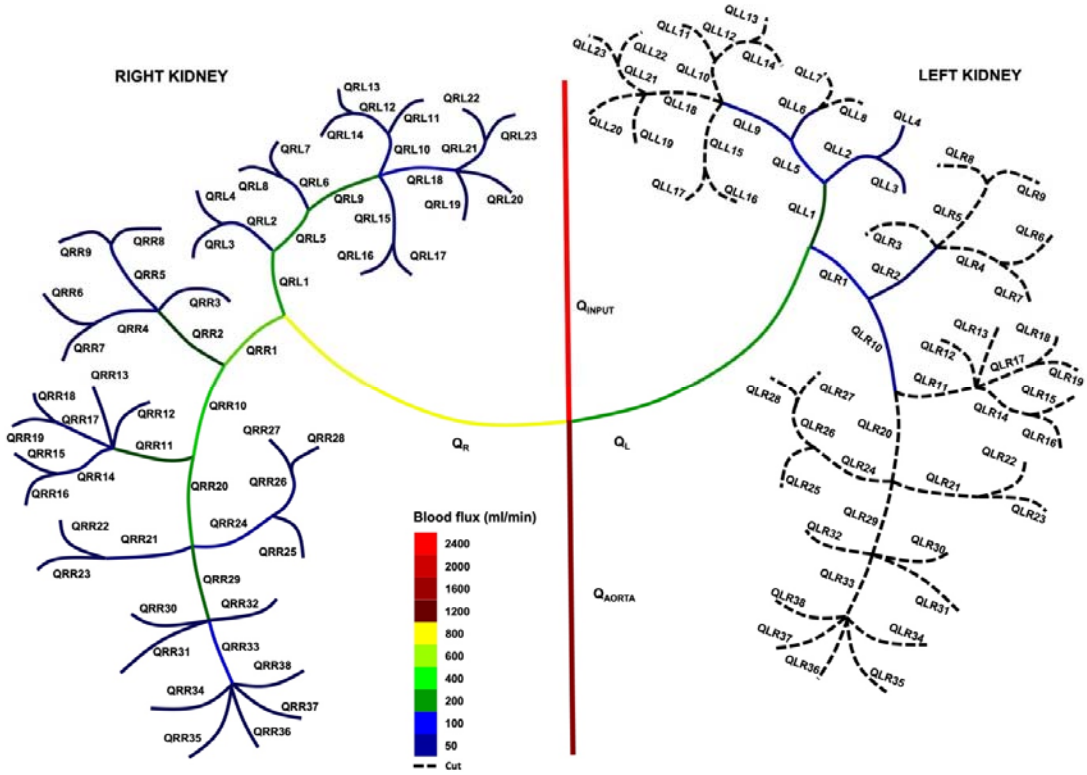

Figure 4. Schematic of the blood flux redistribution due to severing a large portion of the outer regions of the left kidney (around the cortex and medulla), after the nodes Q_{LL6}, Q_{LL9}, Q_{LR2}, and Q_{LR10}, leaving intact the central region (the renal pelvis).

3.4. Mapping the Blood Flux for a Radical Kidney Resection

Figure 5 illustrates the blood loss and blood flux redistribution for a radical kidney resection with the unhealthy kidney's left renal artery experiencing a blood loss of approximately 1.2% of the cardiac output (Table 1). The blood fluxes in the major arteries were Q_L = 59.9 mL/min, Q_R = 837.7 mL/min, and Q_{aorta} = 1502.4 mL/min, with both the aorta and the healthy (right) kidney experiencing significant increases in their blood fluxes (25.12% and 39.71%, respectively). Even though at first glance the right kidney appeared to have a greater % increase than the abdominal aorta, it was calculated that 50.30% of the pre-surgical (healthy) left renal flow was redirected to the aorta, due to its lower impedance, while 39.71% went to the right kidney. This gives a ratio of aortic to right (healthy) kidney redistribution of 1.27 times, which is the same in almost all the nephrectomy scenarios considered (Table 2).

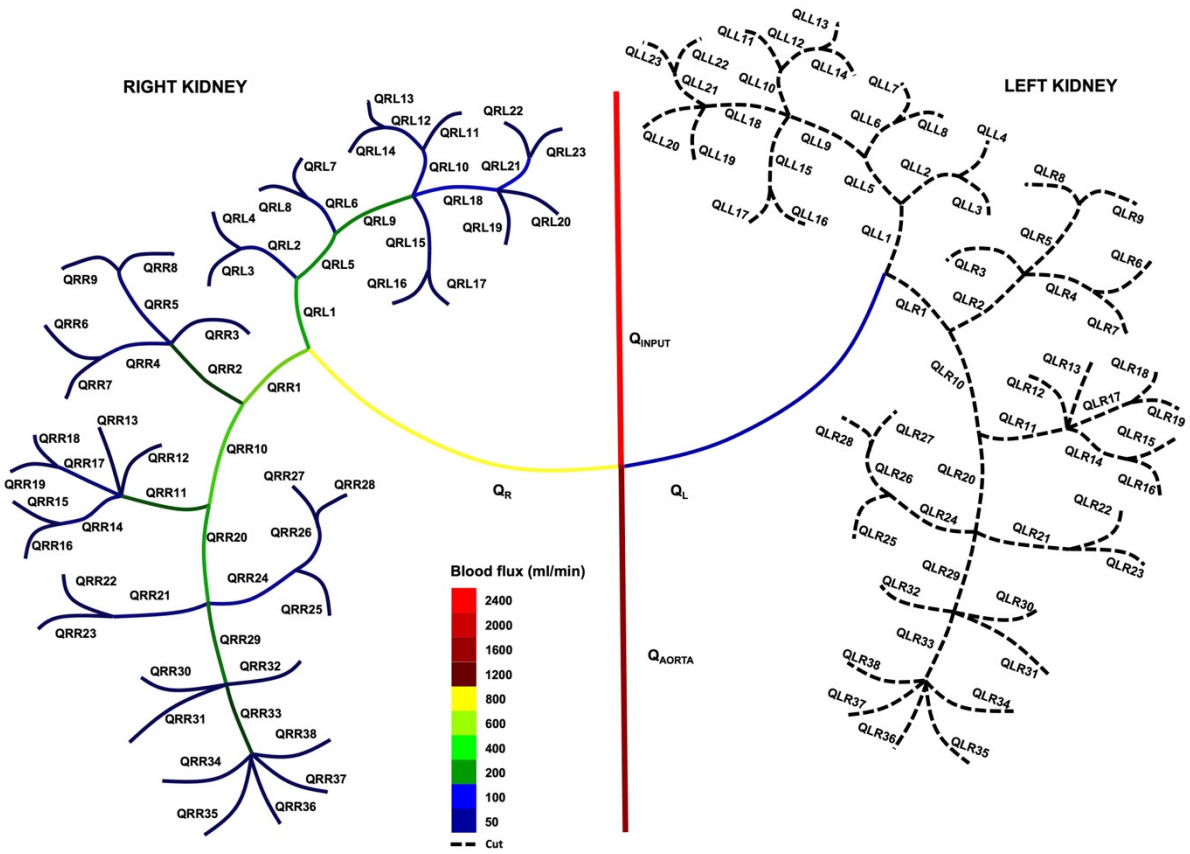

Figure 5. Schematic of the blood flux redistribution between the unhealthy (**left**) kidney, the healthy (**right**) kidney, and the downstream aorta due to a radical left kidney resection with a cut after the node at Q_L, the left major renal artery.

3.5. Blood Pressure Distributions for Pre- and Post-Surgery Nephrectomies

Figure 6 illustrates the various blood pressures in the two-kidney vascular network which are calculated using Equations (1) and (5). The blood pressure, P_{aorta}, at the downstream aorta was significantly lower than P_L or P_R due to the downstream aorta's larger radius which yields a lower impedance (see Table S1).

We next considered the blood pressures in the key major arteries after a variety of cuts to the vascular network. Table 3 illustrates the blood pressures P_R, P_L, and P_{aorta} in the key major arteries after a range of cuts. The blood pressures are calculated using Equations (1) and (5) and using the data from Tables S1 and S2.

Table 3. Blood pressure in the key major arteries P_R, P_L, and P_{aorta} after a variety of cuts.

Branch Cut(s)	Blood Pressure, P_R (mmHg)	Blood Pressure, P_L (mmHg)	Blood Pressure, P_{aorta} (mmHg)
Healthy kidneys (with no cuts)	125.2	125.2	10.3
P_L (radical kidney resection)	175.0	12.5	12.9
P_{LR33}	128.1	118.8	10.5
P_{LR2} & P_{LR10}	150.3	68.4	11.7
P_{LR11} & P_{LR20}	143.1	84.8	11.3
P_{LL2} & P_{LL5}	135.6	101.7	10.9
P_{LL6} & P_{LL9}	133.1	107.3	10.8
P_{LL6} & P_{LL9} & P_{LR2} & P_{LR10}	162.2	41.4	12.3

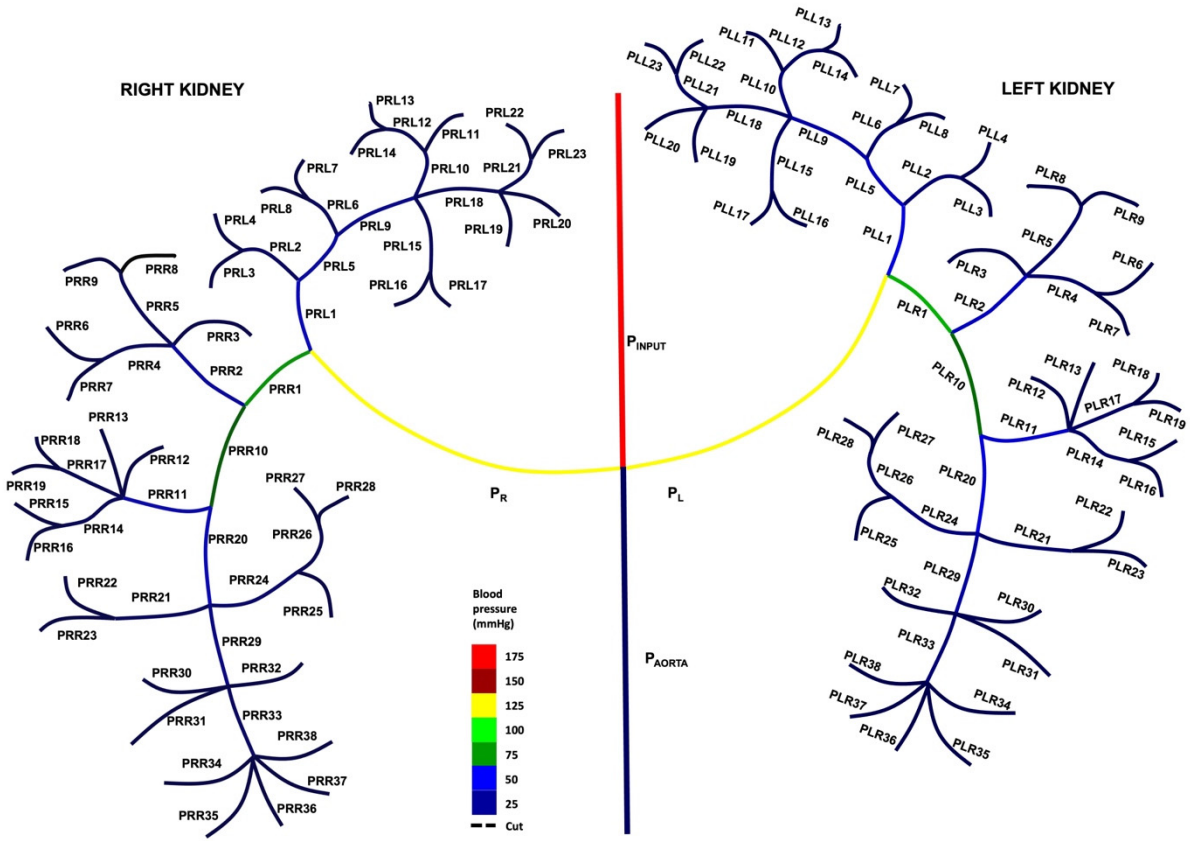

Figure 6. Schematic of the blood pressure distributions for a healthy two-kidney vascular network, before any severing of blood vessels.

Table 3 emphasizes how the blood pressure for the aorta is approximately one order of magnitude lower than the blood pressure for P_R despite the blood flux, Q_{aorta}, being larger in size than Q_R. As various cuts were performed to the diseased kidney, the pressure in that kidney, P_L, was reduced in value (5.11–90.02% reduction) due to the redistribution of blood flux rates. The redistribution of flux to both the aorta and the healthy (right) kidney resulted in an increase in their respective blood pressures with the healthy kidney experiencing a pressure increase of 2.32–39.78% for the cases examined (Table 3), due to its higher impedance compared to the downstream aorta (1.94–25.24% increase).

Figure 7 illustrates the blood pressure redistribution for a particular case where the outer cortex and medulla were severed with cuts being made after the nodes at P_{LL6}, P_{LL9}, P_{LR2}, and P_{LR10}, while the central renal pelvis region was maintained (the equivalent blood flux distribution is shown in Figure 4). Both P_R and P_{aorta} increased in value compared to the healthy two-kidney model shown in Figure 6, with P_R displaying the greater increase in blood pressure (29.55% for P_R vs. 19.42% for P_{aorta}) due to its higher impedance, while the pressure decreased in the left renal artery post-surgically by 66.93%.

Figure 8 highlights how the blood pressure in each blood vessel was redistributed in the healthy (right) kidney and the downstream aorta due to a radical renal resection for a cut being made after the node at P_L. The healthy kidney, P_R, experienced an elevated blood pressure, due to an increase in its flux, with P_R = 175 mmHg (39.78% increase), while P_{aorta} increased by 25.24% to P_{aorta} = 12.9 mmHg due to its lower impedance. The pressure in the left renal artery dropped markedly by 90.02% to 12.5 mmHg.

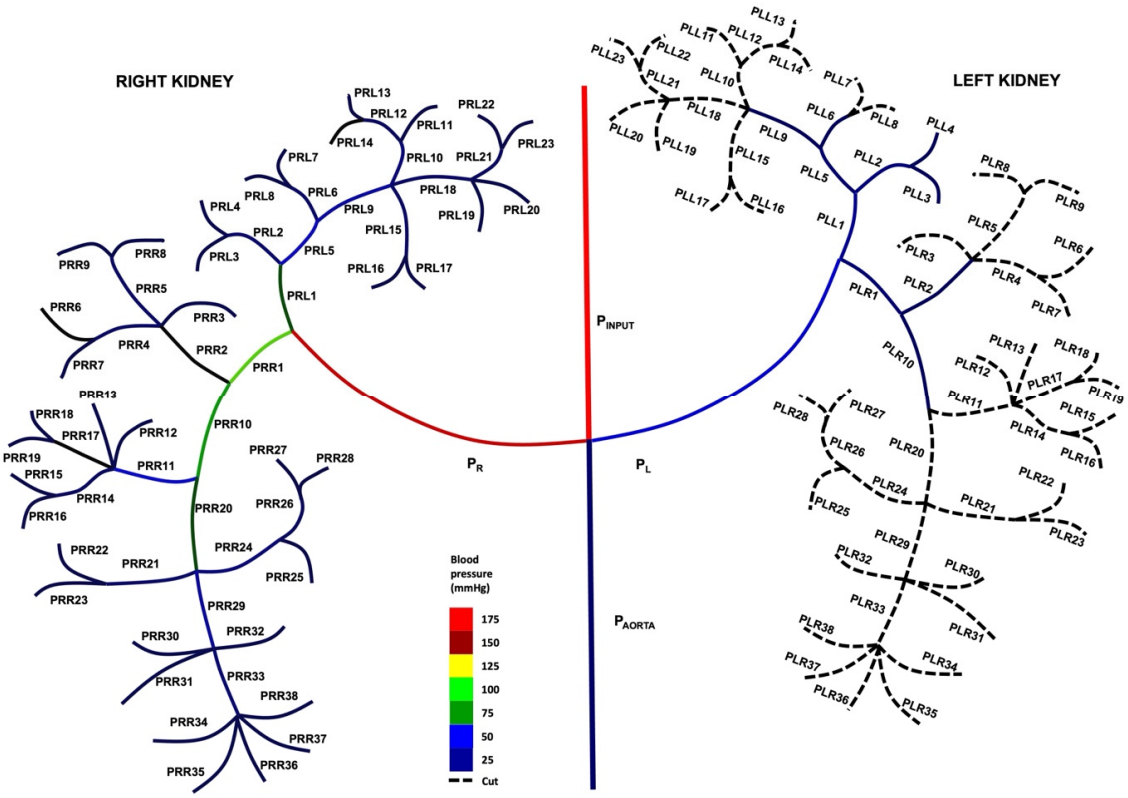

Figure 7. Schematic of the blood pressure redistribution due to cross cutting after the nodes P_{LR2}, P_{LR10}, P_{LL6}, and P_{LL9} for the two-kidney vascular network.

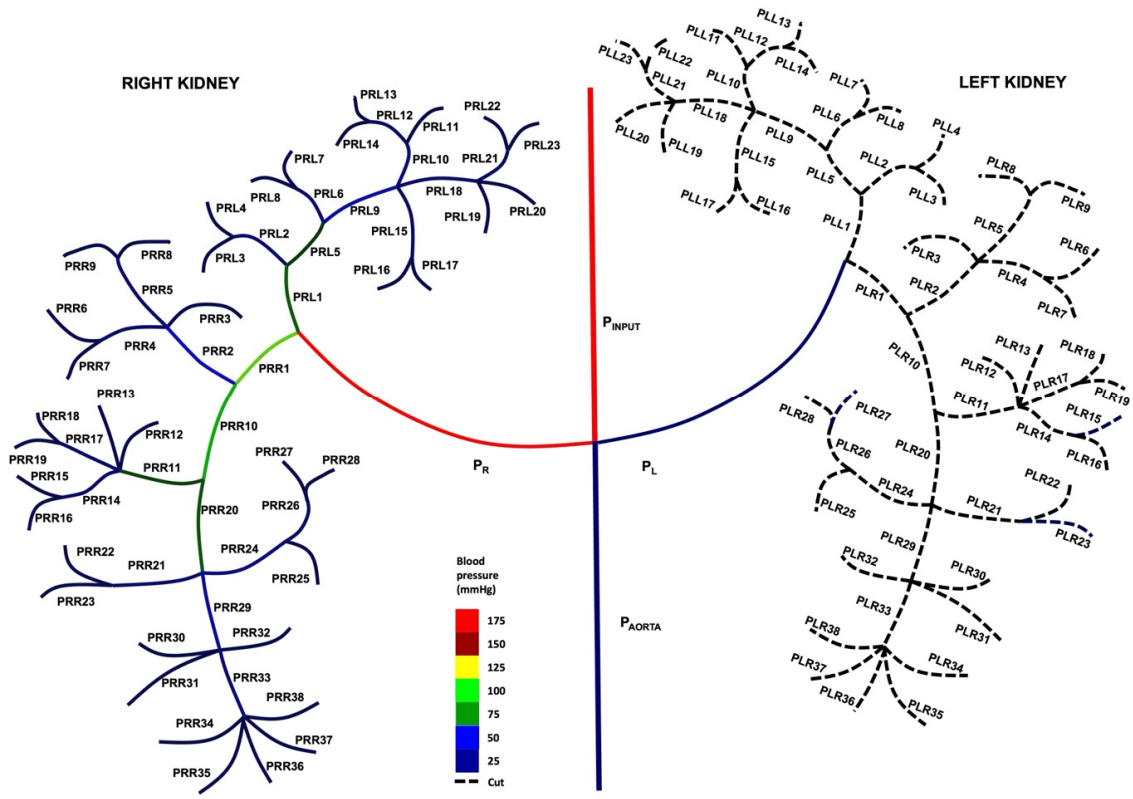

Figure 8. Schematic of the blood pressure redistribution due to a radical left renal resection with the severing of the major renal left artery after the node P_L.

4. Discussion

We developed a novel lumped-parameter mathematical model for a complex two-kidney vascular network, accounting for the non-Newtonian behavior of blood by modelling it as a Carreau fluid. The impedance of each blood vessel was determined using the three-element Windkessel model. Our model's originality is that it can quantify blood loss for a variety of radical or partial unilateral kidney nephrectomy scenarios alongside determining blood fluxes and pressures for each vessel and accounting for changes in the total impedance of the two kidneys. The left kidney was used in this work as the diseased one, but due to the assumed symmetry of the network, the results would be the same if the surgery concerned the right kidney. We showed that cutting a vessel or several vessels results in a redistribution of the blood fluxes and pressures from the diseased kidney to the downstream aorta and the healthy kidney, with the aorta receiving an approximately 1.27 times higher blood flux redistribution compared to the healthy kidney due to its wider radius and therefore lower impedance. Severing blood vessels in any part of the kidney vascular network increases the impedance in that region of the altered kidney which results in a redistribution of the blood flux to the areas of the two-kidney model that exhibit a lower impedance. This redistribution of the blood flux also leads to changes in blood pressure via Ohm's law, with higher blood pressures occurring in both the aorta output and the healthy kidney. Rosiello et al. [1] showed that there is a strong correlation between blood losses of over 500 mL and the onset of chronic kidney disease. Our model calculated a blood loss rate of 150.7 mL/min for cuts after the nodes at Q_{LL6}, Q_{LL9}, Q_{LR2}, and Q_{LR10} implying that failing to stem the bleeding in a time frame of approximately 4 min may increase the risk of the patient developing chronic kidney disease. Shvarts et al. [67] assessed the blood losses associated with radical nephrectomy due to renal cell carcinoma and measured blood losses in the range of 200 to 555 cc. Our model predicts a blood loss of 59.9 mL/min when the branch Q_L is cut which implies minimal and maximal bleeding times of approximately between 3 and 9 min, respectively, if the surgical procedure is performed off-clamp. To the best of the authors' knowledge, this is the first model capable of estimating the perfusion in both kidneys' vasculatures and the abdominal aorta and of providing fast and efficient calculations of blood loss due to surgery, which has a clear clinical significance.

4.1. Clinical Relevance

The clinical relevance of this model lies in the management of blood flow and blood loss related to kidney surgeries, particularly nephrectomies. The primary surgical treatments for renal cancer include radical and partial nephrectomy, which can be performed laparoscopically or through open surgery. Recently, robotic-assisted partial nephrectomy gained prominence and is considered a gold standard in the field. A critical aspect of these surgeries is accurately mapping the blood vessels, as their configurations can vary significantly from patient to patient. Variations in the renal artery, renal vein, and surrounding vessels can complicate both the planning and execution of the surgery [68,69]. The proximity of the blood vessels to the tumors requires extensive planning due to the risk of significant bleeding during resection. Additionally, the tumors often develop their own extensive blood supply, which can be prone to further bleeding. Effective control of the bleeding is crucial, and surgeons must be prepared with strategies for rapid hemorrhage management, including vessel clamping, use of hemostatic agents, or even transitioning to a partial or radical nephrectomy if necessary [70,71].

The model developed in this work aims to assist surgeons by predicting the blood loss for different types of nephrectomies (partial or radical) and specific blood vessel cuts. Understanding which vessels, when cut, will lead to minimal blood loss can help guide surgeons and potentially reduce overall surgical risks. Furthermore, this model can be integrated into surgical navigation systems and intraoperative monitoring systems to provide real-time feedback on the blood flow and pressure redistributions during the surgery, allowing for dynamic adjustments to minimize blood loss and optimize patient outcomes. It also serves as a valuable educational and training tool, offering surgeons a

deeper understanding of renal hemodynamics and the implications of different surgical techniques [72]. The model has a direct potential to be used in a real clinical environment due to its fast processing speed, thus allowing surgeons to access the relevant data rapidly and efficiently. Incorporating this model in advanced planning tools, such as virtual reality (VR) systems, could predict areas of high risk for significant blood loss, leading to more personalized and less invasive surgical approaches.

This model can further be incorporated into surgical training programs, where trainees can use it to simulate different nephrectomy scenarios and learn how various surgical decisions impact blood flow and patient outcomes. This hands-on experience can improve decision-making skills and preparedness for real surgeries. By implementing this model in real-world practice, surgeons can enhance their decision-making process, reduce risks, and improve outcomes for patients undergoing kidney surgeries.

This model has, thus, the capacity to improve the efficacy of renal surgery by identifying the appropriate pre-surgical protocols required to minimize blood loss to below the threshold of 500 mL [1]. The results of this study on expected blood loss rates can guide surgeons as to whether an off-clamp partial or radical nephrectomy is both safe and pragmatically feasible. This model also highlights the regions of the vascular network where tissue necrosis is more likely due to high blood loss and subsequent oxygen deprivation [73].

4.2. Limitations

We made several key assumptions in the presented model, based on extremely limited clinical data obtained via a thorough literature search. The vessel lengths, radii, and impedances in the complex human two-kidney vascular network were based on approximations, particularly the lengths being all equal in size since the primary and secondary blood vessels are of a similar order of magnitude. However, a previous sensitivity analysis by [55] showed minimal influence of these variables on the flux rate calculation; thus, more precise anatomical data are not expected to modify the results of the present model. Further, our model neglected the viscoelastic behavior of blood vessels, considering they were rigid. This assumption was made to simplify the modelling, primarily due to the complexity and scale of the two-kidney vasculature.

The presented model was designed to focus on short post-severing time intervals, since we are primarily interested in the immediate, transient blood loss at the initial point of cutting. This study did not consider extended post-surgery time intervals since these would result in significant blood losses, which could be controlled and minimized locally by the renal surgeon (s). The short post-cutting time intervals assumption implies that the influence of autoregulation [14,15] and coagulation [74] can be neglected since both these processes necessitate longer time frames. In addition, the model assumed a steady blood flow; however, we do not anticipate major differences with using unsteady flow since pulsatility attenuates further downstream in the periphery [75].

The human body is inherently a complex system with multiple interconnected vascular networks. Using a fully three-dimensional computational model of such a complex vascular network would be memory intensive and computationally costly. It would extend the calculation times considerably, making it inefficient and impractical to implement in a real-world clinical setting.

There is further the assumption that the left and right kidney are identical in the presented model. There are anatomical and physiological differences between left and right kidneys that could affect model predictions. These differences include variations in size, position, blood supply, and the presence of congenital anomalies. For instance, the left kidney is typically slightly larger and positioned slightly higher (proximally) than the right kidney due to the presence of the liver on the right side. The left kidney has been reported to be around 10–15% larger than the right kidney in terms of volume [76]. Furthermore, the superior mesenteric artery, which originates superiorly from the renal arteries, was not included in the model. Further refinements are therefore necessary for personalized

medicine. Incorporating patient-specific data into the model could enhance its accuracy and clinical applicability. Future research could focus on documenting and integrating these variations to improve the model's predictive power in diverse clinical scenarios.

4.3. Future Work

Future research will focus on procuring more accurate data by utilizing clinical information obtained via both magnetic resonance imaging and high-frequency ultrasound in conjunction with ultrasound contrast agents as discussed by Kalantarinia et al. [10]. Accessing rigorous clinical data such as the pulse velocities, radii, and lengths of the numerous arteries will allow accurate determination of the impedances and compliances as discussed by Hyde-Linaker et al. [44]. Future work will also include the effects of viscoelasticity in our vascular network model via numerical analysis techniques as discussed by Piccioli et al. and Watanabe et al. [43,77]. Another future direction is to extend our current work from a lumped-parameters first approximation to a 1D time-evolving model with viscoelasticity that accounts for time evolution of the blood vessels, cross-sectional areas, and blood flux rates based on clinical data obtained via extensive medical imaging. A further potential area of future research is to construct a mathematical model that accurately accounts for asymmetry in the two-kidney network in conjunction with rigorous clinical data obtained via medical imaging. A physical model (phantom) of the two-kidney vascular network could also be developed to compare with our mathematical model. Finally, another potential area of future work is the employment of advanced microfluidic systems which may provide a more systematic approach to both computation and validation. Such systems would allow for a detailed study of the microvascular environment surrounding tumors; however, their implementation would be challenging in a clinical setting with respect to both space and processing time.

5. Conclusions

We present, for the first time, a novel mathematical lumped-parameter model of a complex vascular network, specifically addressing the vasculatures of the two kidneys and the abdominal aorta, which enables near real-time estimation of the blood loss and flow–pressure redistributions arising from various scenarios of radical or partial unilateral nephrectomy. The model accounts for the transient change in the total impedance of the two-kidney vasculature immediately following the severing of multiple blood vessels, prior to any autoregulation recovery or blood coagulation. While acknowledging the limitations of our model (see Section 4.2), a significant finding is that in nearly all examined cases, the downstream aorta received an approximately 1.27 times higher percentage of the redistributed flow from the diseased kidney compared to that received by the healthy kidney. Future work will focus on acquiring more accurate clinical data and on further refining the modelling assumptions (see Section 4.3).

Usage of this model allows a fast estimation of the blood loss due to the severing of blood vessels and can help renal surgeons determine the need for intraoperative arterial clamping or preoperative embolization, which can effectively limit bleeding in high-risk cases, thus allowing minimization of potential cellular necrosis. The presented model can be applied to real-life scenarios, such as in robotic partial nephrectomy, where detailed planning using 3D models has been shown to improve surgical outcomes, reduce conversion rates to radical nephrectomy, and lower blood loss [78]. The model's predictive capability is crucial, particularly for patients with compromised renal function, as excessive blood loss can further exacerbate kidney health deterioration and increase the risk of post-surgery chronic kidney disease. This comprehensive mathematical model has the potential to enhance surgical precision, guiding surgeons in selecting the most appropriate procedure for individual patients and optimizing patient recovery.

Supplementary Materials: The following supporting information can be downloaded at: https://www.mdpi.com/article/10.3390/fluids9090214/s1.

Author Contributions: J.C. and A.K.: formal analysis, methodology, software, writing—original draft, investigation, validation, data curation, writing—review and editing, visualization. A.K.: supervision, writing—review. G.D.S. and J.K.: writing—review and editing on clinical relevance. A.K., G.D.S., X.L. and W.S.: funding acquisition. A.K., W.S. and X.L.: conceptualization, review, project administration. All authors have read and agreed to the published version of the manuscript.

Funding: The authors would like to gratefully acknowledge the financial support provided by the UK Research and Innovation (UKRI) Engineering and Physical Sciences Research Council (EPSRC), Transformative Healthcare Technologies Award Ref EP/W004860/1 and EP/X033686/1.

Data Availability Statement: The scientific data underpinning this journal publication is openly available from the University of Strathclyde Knowledge Base. DOI repository https://doi.org/10.15129/6f56502c-62bf-47b2-9208-6c41814ca50a.

Conflicts of Interest: The authors declare that the research was conducted in the absence of any commercial or financial relationships that could be construed as a potential conflict of interest.

Nomenclature

μCT, micro-computed tomography; φ, hematocrit; ω, angular frequency; C_k, compliance of the blood vessel; CO, cardiac output; L, left; LL1, the first left branch of the left renal artery; LR1, the first right branch of the left renal artery; LR4, LR6, and LR7, branches labelled on the right branching of the left renal artery; MRI, Magnetic Resonance Imaging; OPT, optical projection tomography; P_{aorta}, blood pressure at the downstream aorta; ΔP_k, pressure gradient in blood vessel k; P_k, pressure; P_L, pressure in the left renal artery; P_0, pressure amplitude; P_R, pressure in the right renal artery; Q_{aorta}, inlet flow rate in the abdominal aorta; Q_k, the flux of blood vessel k; Q_L, the flux in the left renal artery; Q_R, the flux in the right renal artery; R, right; RL1, the first left branch of the right renal artery; RR1, the first right branch of the right renal artery; t, time; ΔV_k, change in vessel volume; UCAs, ultrasound contrast agents; Z_k, impedance of the blood vessel; Z_{k1} and Z_{k2}, resistors of the three-element Windkessel model.

References

1. Rosiello, G.; Larcher, A.; Fallara, G.; Basile, G.; Cignoli, D.; Colandrea, G.; Re, C.; Trevisani, F.; Karakiewicz, P.I.; Salonia, A.; et al. The impact of intraoperative bleeding on the risk of chronic kidney disease after nephron-sparing surgery. *World J. Urol.* **2021**, *39*, 2553–2558. [CrossRef] [PubMed]
2. Bivet, F. Nonuse of RIFLE classification urine output criteria: Biases for acute kidney injury biomarkers performance assessment? *Crit. Care Med.* **2012**, *40*, 1692–1693. [CrossRef] [PubMed]
3. Kanji, H.D.; Schulze, C.J.; Hervas-Malo, M. Difference between pre-operative and cardiopulmonary bypass mean arterial pressure is independently associated with early cardiac surgery-associated acute kidney injury. *J. Cardiothorac. Surg.* **2010**, *5*, 1–9. [CrossRef] [PubMed]
4. Robert, A.M.; Kramer, R.S.; Dacey, L.I. Cardiac surgery-associated acute kidney injury: A comparison of two consensus criteria. *Ann. Thorac. Surg.* **2010**, *90*, 1939–1943. [CrossRef]
5. Weir, M.R.; Aronson, S.; Avery, E.G. Acute kidney injury following cardiac surgery: Role of perioperative blood pressure control. *Am. J. Nephrol.* **2011**, *33*, 438–452. [CrossRef]
6. Jaramillo, S.; Muntane, M.M.; Gambus, P.L.; Capitan, D.; Navarro-Ripoll, R.; Blasi, A. Perioperative blood loss: Estimation of blood volume loss or haemoglobin mass loss? *Blood Transfus.* **2020**, *18*, 20–29.
7. Puelles, V.G.; Combes, A.N.; Bertram, J.F. Clearly imaging and quantifying the kidney in 3D. *Kidney Int.* **2021**, *100*, 780–786. [CrossRef]
8. Schutter, R.; Lantinga, V.A.; Hamelink, T.L.; Pool, M.B.F.; Varsseveld, O.C.V.; Potze, J.H.; Hillebrands, J.L.; Heuvel, M.C.V.D.; Dierckx, R.A.J.O.; Leuvenink, H.G.D.; et al. Magnetic resonance imaging assessment of renal flow distribution patterns during ex vivo normothermic machine perfusion in porcine and human kidneys. *Transpl. Int.* **2021**, *34*, 1643–1655. [CrossRef]
9. Nordsletten, D.A.; Blackett, S.; Bentley, M.D.; Ritman, E.L.; Smith, N.P. Structural morphology of renal vasculature. *Am. Physiol. Soc.* **2006**, *291*, 296–309. [CrossRef]
10. Kalantarinia, K.; Belcik, J.T.; Patrie, J.T.; Wei, K. Real-time measurement of renal blood flow in healthy subjects using contrast-enhanced ultrasound. *Am. J. Physiol. Ren. Physiol.* **2009**, *297*, 1129–1134. [CrossRef]
11. Cowley, J.; McGinty, S. A mathematical model of sonoporation using a liquid-crystalline shelled microbubble. *Ultrasonics* **2019**, *96*, 214–219. [CrossRef] [PubMed]
12. Cowley, J.; Mulholland, A.J.; Gachagan, A. The Rayleigh-Plesset equation for a liquid-crystalline shelled microbubble. *Int. J. Mod. Eng. Res. IJMER* **2020**, *10*, 25–35.

13. Lok, C.E.; Huber, T.S.; Lee, T.; Shenoy, S.; Yevzlin, A.S.; Abreo, K.; Allon, M.; Asif, A.; Astor, B.C.; Glickman, M.H.; et al. Kdoqi clinical practice guideline for vascular access: 2019 update. *Am. J. Kidney Dis.* **2020**, *75*, 1–164. [CrossRef] [PubMed]
14. Cupples, W.; Loutzenhiser, R. Dynamic autoregulation in the in vitro perfused hydronephrotic rat kidney. *Am. J. Physiol. Ren. Physiol.* **1998**, *275*, 126–130. [CrossRef]
15. Cupples, W.A.; Braam, B. Assessment of renal autoregulation. *Am. J. Physiol. Ren. Physiol.* **2007**, *292*, 1105–1123. [CrossRef]
16. Holstein-Rathlon, N.H.; Marsh, D.J. A dynamic model of renal blood flow autoregulation. *Bull. Math. Biol.* **1994**, *56*, 411–429. [CrossRef]
17. Holstein-Rathlou, N.; Wagner, A.; Marsh, D. Tubloglomerular feedback dynamics and renal blood flow autoregulation in rats. *Am. J. Physiol. Ren. Physiol.* **1991**, *260*, 53–68. [CrossRef]
18. Just, A. Mechanisms of renal blood flow autoregulation: Dynamics and contributions. *Am. J. Physiol. Regul. Integr. Comp. Physiol.* **2007**, *292*, R1–R17. [CrossRef]
19. Just, A.; Arendshorst, W.J. Dynamics and contribution of mechanisms mediating renal blood flow autoregulation. *Am. J. Physiol. Regul. Integr. Comp. Physiol.* **2003**, *285*, 619–631. [CrossRef]
20. Loutzenhiser, R.; Bidani, A.; Chilton, L. Renal myogenic response: Kinetic attributes and physiological role. *Circ. Res.* **2002**, *90*, 1316–1324. [CrossRef]
21. Loutzenhiser, R.; Griffin, K.; Williamson, G.; Bidani, A. Renal autoregulation: New perspectives regarding the protective and regulatory roles of the underlying mechanisms. *Am. J. Physiol. Regul. Integr. Comput. Physiol.* **2006**, *290*, 1156–1167. [CrossRef] [PubMed]
22. Lush, D.J.; Fray, J.C. Steady-state autoregulation of renal blood flow: A myogenic model. *Am. J. Physiol. Regul. Integr. Comput. Physiol.* **1984**, *247*, 89–99. [CrossRef] [PubMed]
23. Marsh, D.; Sosnovtseva, O.; Chon, K.; Holstein-Rathlou, N. Nonlinear interactions in renal blood blow regulation. *Am. J. Physiol. Regul. Integr. Comp. Physiol.* **2005**, *288*, 1143–1159. [CrossRef] [PubMed]
24. Marsh, D.; Sosnovtseva, O.; Mosekilde, E.; Holstein-Rathlou, N. Vascular coupling induces synchronization, quasiperiodicity, and chaos in a nephron tree. *Chaos* **2007**, *17*, 015114. [CrossRef] [PubMed]
25. Marsh, D.; Sosnovtseva, O.; Pavlov, A.; Yip, K.; Holstein-Rathlou, N. Frequency encoding in renal blood blow regulation. *Am. J. Physiol. Regul. Integr. Comp. Physiol.* **2005**, *288*, 1160–1167. [CrossRef]
26. Moore, L. Tubuloglomerular feedback and SNGFR autoregulation in the rat. *Am. J. Physiol. Ren. Physiol.* **1984**, *247*, 267–276. [CrossRef]
27. Oien, A.H.; Aukland, K. A mathematical-analysis of the myogenic hypothesis with special reference to auto-regulation of renal blood-flow. *Circ. Res.* **1983**, *52*, 241–252. [CrossRef]
28. Persson, P. Renal blood flow autoregulation in blood pressure control. *Curr. Opin. Nephrol. Hypertens.* **2002**, *11*, 67–72. [CrossRef]
29. Pires, S.L.S.; Julien, C.; Chapuis, B.; Sassard, J.; Barres, C. Spontaneous renal blood flow autoregulation curves in conscious sinoaortic baroreceptor-denervated rats. *Am. J. Physiol. Ren. Physiol.* **2002**, *282*, 51–58. [CrossRef]
30. Racasan, S.; Joles, J.; Boer, P.; Koomans, H.; Braam, B. NO dependency of RBF and autoregulation in the spontaneously hypertensive rat. *Am. J. Physiol. Ren. Physiol.* **2003**, *285*, 105–112. [CrossRef]
31. Turkstra, E.; Braam, B.; Koomans, H. Impaired renal blood flow autoregulation in twokidney, one-clip hypertensive rats is caused by enhanced activity of nitric oxide. *J. Am. Soc. Nephrol.* **2000**, *11*, 847–855. [CrossRef]
32. Cury, L.F.M.; Talou, G.M.; Younes-Ibrahim, M.; Blanco, P.J. Parallel generation of extensive vascular networks with application to an archetypal human kidney model. *R. Soc. Open Sci.* **2021**, *8*, 210973. [CrossRef]
33. Deng, W.; Tsubota, K.I. Numerical simulation of the vascular structure dependence of blood flow in the kidney. *Med. Eng. Phys.* **2022**, *104*, 103809. [CrossRef]
34. Deng, W.; Tsubota, K.I. Numerical Modeling and Simulation of Blood Flow in a Rat Kidney: Coupling of the Myogenic Response and the Vascular Structure. *Processes* **2022**, *10*, 1005. [CrossRef]
35. Sgouralis, I.; Evans, R.G.; Layton, A.T. Renal medullary and urinary oxygen tension during cardiopulmonary bypass in the rat. *Math. Med. Biol.* **2017**, *34*, 313–333. [CrossRef]
36. Sgouralis, I.; Layton, A.T. Mathematical modeling of renal hemodynamics in physiology and pathophysiology. *Math. Biosci.* **2015**, *264*, 8–20. [CrossRef]
37. Postnov, D.D.; Marsh, D.J.; Postnov, D.E.; Braunstein, T.H.; Holstein-Rathlou, N.H.; Martens, E.A.; Sosnovtseva, O. Modeling of Kidney Hemodynamics: Probability-Based Topology of an Arterial Network. *PLoS Comput. Biol.* **2016**, *12*, e1004922. [CrossRef]
38. Hao, W.; Rovin, B.H.; Friedman, A. Mathematical model of renal interstitial fibrosis. *Proc. Natl. Acad. Sci. USA* **2014**, *111*, 14193–14198. [CrossRef]
39. Basri, A.A.; Khader, S.M.A.; Johny, C.; Pai, B.R.; Zuber, M.; Ahmad, Z.; Ahmad, K.A. Effect of Single and Double Stenosed on Renal Arteries of Abdominal Aorta: A Computational Fluid Dynamics. *CFD Lett.* **2020**, *12*, 87–97.
40. Grinberg, L.; Cheever, E.; Anor, T.; Madsen, J.R.; Karniadakis, G.E. Modeling blood flow circulation in intracranial arterial networks: A comparative 3D/1D simulation study. *Ann. Biomed. Eng.* **2011**, *39*, 297–309. [CrossRef]
41. Grinberg, L.; Karniadakis, G.E. Outflow boundary conditions for arterial networks with multiple outlets. *Ann. Biomech. Eng.* **2008**, *36*, 1496–1514. [CrossRef] [PubMed]
42. Kamiya, A.; Togawa, T. Optimal branching structure of the vascular tree. *Bull. Math. Biophys.* **1972**, *34*, 431–438. [CrossRef] [PubMed]

43. Watanabe, S.M.; Blanco, P.J.; Feijóo, R.A. Mathematica Model of Blood Flow in an Anatomically Detailed Arterial Network of the Arm. *ESAIM Math. Model. Numer. Anal.* **2013**, *47*, 961–985. [CrossRef]
44. Hyde-Linaker, G.; Barientos, P.H.; Stoumpos, S.; Kingsmore, D.B.; Kazakidi, A. Patient-specific computational haemodynamics associated with the surgical creation of an arteriovenous fistula. *Med. Eng. Phys.* **2022**, *105*, 103814. [CrossRef]
45. Black, S.M.; Maclean, C.; Hall-Barrientos, P.; Ritos, K.; McQueen, A.; Kazakidi, A. Calibration of patient-specific boundary conditions for coupled CFD models of the aorta derived from 4D Flow-MRI. *Front. Bioeng. Biotech.* **2023**, *11*, 1178483.
46. Boumpouli, M.; Danton, M.H.D.; Gourlay, T.; Kazakidi, A. Blood flow simulations in the pulmonary bifurcation in relation to adult patients with repaired tetralogy of Fallot. *Med. Eng. Phys.* **2020**, *85*, 123–138.
47. Johnston, L.; Allen, R.; Hall Barrientos, P.; Mason, A.; Kazakidi, A. Hemodynamic abnormalities in the aorta of turner syndrome girls. *Front. Cardiovasc. Med.* **2021**, *8*, 670841.
48. Kazakidi, A.; Sherwin, S.J.; Weinberg, P.D. Effect of Reynolds number and flow division on patterns of haemodynamic wall shear stress near branch points in the descending thoracic aorta. *J. R. Soc. Interface* **2009**, *6*, 539–548. [CrossRef]
49. Doormaal, M.A.V.; Kazakidi, A.; Wylezinska, M.; Hunt, A.; Tremoleda, J.L.; Protti, A.; Bohraus, Y.; Gsell, W.; Weinberg, P.D.; Ethier, C.R. Haemodynamics in the mouse aortic arch computed from MRI-derived velocities at the aortic root. *J. R. Soc. Interface* **2012**, *9*, 2834–2844.
50. Kazakidi, A.; Plata, A.M.; Sherwin, S.J.; Weinberg, P.D. Effect of reverse flow on the pattern of wall shear stress near arterial branches. *J. R. Soc. Interface* **2011**, *8*, 1594–1603. [CrossRef]
51. Pedley, T.J.; Schroter, R.C.; Sudlow, M.F. Flow and pressure drop in systems of repeatedly branching tubes. *J. Fluid Mech.* **1971**, *46*, 365–383. [CrossRef]
52. Shi, Y.; Lawford, P.; Hose, R. Review of Zero-D and 1-D models of blood flow in the cardiovascular system. *BioMed. Eng. OnLine* **2011**, *10*, 33. [CrossRef] [PubMed]
53. Cowley, J.; Luo, X.; Stewart, G.D.; Shu, W.; Kazakidi, A. A mathematical model of blood loss during renal resection. *Fluids* **2023**, *8*, 316. [CrossRef]
54. Sherman, T.F. On connecting large vessels to small. The meaning of Murray's law. *J. Gen. Physiol.* **1981**, *78*, 431–453. [CrossRef]
55. Yang, J.; Pak, Y.E.; Lee, T.-R. Predicting bifurcation angle effect on blood flow in the microvasculature. *Microvasc. Res.* **2016**, *108*, 22–28. [CrossRef]
56. Bessonov, N.; Sequeira, A.; Simakov, S.; Vassilevskii, Y.; Volpert, V. Methods of blood flow modelling. *Math. Model. Nat. Phenom.* **2016**, *11*, 1–25. [CrossRef]
57. Aroesty, J.; Gross, J.F. The mathematics of pulsatile flow in small vessels I. Casson theory. *Microvasc. Res.* **1972**, *4*, 1–12. [CrossRef]
58. Paruchuri, V.; Salhab, K.F.; Kuzmik, G.; Gubernikoff, G.; Fang, H.; Rizzo, J.A.; Ziganshin, B.A.; Elefteriades, J.A. Aortic Size Distribution in the General Population: Explaining the Size Paradox in Aortic Dissection. *Cardiology* **2015**, *131*, 265–272. [CrossRef]
59. Stark, H.; Schuster, S. Comparison of various approaches to calculating the hematocrit in vertebrates. *J. Appl. Physiol.* **2012**, *113*, 355–367. [CrossRef]
60. Sochi, T. Analytical solutions for the flow of Carreau and Cross fluids in circular pipes and thin slits. *Rheol. Acta* **2015**, *54*, 745–756. [CrossRef]
61. Wolfram Inc. *Mathematica, Version 130*; Wolfram Inc.: Champaign, IL, USA, 2022.
62. Zhao, Y.; Lieber, B. Steady inspiratory flow in a model symmetric bifurcation. *J. Biomech. Eng.* **1994**, *116*, 488–496. [CrossRef] [PubMed]
63. Schroter, R.C.; Sudlow, M.F. Flow patterns in models of the human bronchial airways. *Respir. Physiol.* **1969**, *7*, 341–355. [CrossRef] [PubMed]
64. López-Picado, A.; Albinarrate, A.; Barrachina, B. Determination of perioperative blood loss: Accuracy or approximation? *Anesth. Analg.* **2017**, *125*, 280–286. [CrossRef] [PubMed]
65. Abu-Naser, M.; Williamson, G.A.; Bidani, A.K.; Griffin, K.A. Vascular resistance estimation in real hemodynamics using a time-varying Windkessel model. In Proceedings of the Proceedings. (ICASSP '05), IEEE International Conference on Acoustics, Speech, and Signal Processing, 2005, Philadelphia, PA, USA, 23 March 2005; Volume 5, pp. 641–644.
66. Hsu, T.L.; Hsiu, H.; Chao, P.T.; Li, S.P.; Wang, W.K.; Wang, Y.Y.L. Three-block electrical model of renal impedance. *IOP Physiol. Meas.* **2005**, *26*, 387–399. [CrossRef]
67. Shvarts, O.; Tsui, K.; Smith, R.B.; Kernion, J.B.D.; Belldegrun, A. Blood loss and the need for transfusion in patients who undergo partial or radical nephrectomy for renal cell carcinoma. *J. Urol.* **2000**, *164*, 1160–1163. [CrossRef]
68. Aboumarzouk, O.M.; El-Damanhoury, H.M. The impact of renal vascular anatomy on laparoscopic partial nephrectomy. *J. Endourol.* **2014**, *28*, 438–444.
69. Liu, X.; Fong, Y. Management of renal vascular anatomy during partial nephrectomy. *Urol. Clin. N. Am.* **2013**, *40*, 325–332.
70. Kumar, P.; Ghosh, S. Techniques and strategies in managing hemorrhage during nephrectomy. *J. Urol.* **2018**, *199*, 391–398.
71. Serrano, P.; Khan, M.S. Advances in the management of bleeding during renal surgery. *Expert Rev. Anticancer Ther.* **2015**, *15*, 1415–1424.
72. Kawaguchi, A.; Vigneswaran, H.T. The role of predictive modeling in optimizing surgical outcomes: A review. *J. Surg. Res.* **2017**, *218*, 94–104.
73. Warren, D.R.; Partridge, M. The role of necrosis, acute hypoxia and chronic hypoxia in ^{18}F-FMISO PET image contrast: A computational modelling study. *Phys. Med. Biol.* **2016**, *61*, 8596–8624. [CrossRef] [PubMed]

74. Andreeva, A.A.; Anand, M.; Lobanov, A.I.; Nikolaev, A.V.; Panteleev, M.A.; Susree, M. Mathematical modelling of platelet rich plasma clotting. Pointwise unified model. *Russ. J. Numer. Anal. Math. Model.* **2018**, *33*, 265–276. [CrossRef]
75. Salotto, A.G.; Muscarella, L.F.; Melbin, J.; Li, J.K.J.; Noordergraaf, A. Pressure pulse transmission into vasculare beds. *Microvasc. Res.* **1986**, *32*, 152–163. [CrossRef] [PubMed]
76. Soares, T.R.S.; Ferraz, J.S.; Dartibale, C.B.; Oliveira, I.R.M. Variations in human renal arteries. *Acta Sci. Biol. Sci.* **2013**, *35*, 277–282. [CrossRef]
77. Piccioli, F.; Bertaglia, G.; Valiani, A.; Caleffi, V. Modeling blood flow in networks of viscoelastic vessels with the 1-D augmented fluid–structure interaction system. *J. Comput. Phys.* **2022**, *464*, 111364. [CrossRef]
78. Bianchi, L.; Cercenelli, L.; Bortolani, B.; Piazza, P.; Droghetti, M.; Boschi, S.; Gaudiano, C.; Carpani, G.; Chessa, F.; Lodi, S.; et al. 3D renal model for surgical planning of partial nephrectomy: A way to improve surgical outcomes. *Front. Oncol.* **2022**, *12*, 1046505. [CrossRef]

Disclaimer/Publisher's Note: The statements, opinions and data contained in all publications are solely those of the individual author(s) and contributor(s) and not of MDPI and/or the editor(s). MDPI and/or the editor(s) disclaim responsibility for any injury to people or property resulting from any ideas, methods, instructions or products referred to in the content.